Industrial Chemistry & Materials

ROYAL SOCIETY OF CHEMISTRY

PAPER

View Article Online
View Journal | View Issue

Cite this: *Ind. Chem. Mater.*, 2024, **2**, 321

Exploration of structure sensitivity of gold nanoparticles in low-temperature CO oxidation†

Lei Ying,[ab] Yu Han,[ab] Beien Zhu *[ac] and Yi Gao *[acd]

Gold nanoparticles (NPs) exhibit remarkable catalytic activity in low-temperature CO oxidation and their performance is highly dependent on size and shape. However, the underlying mechanism isn't fully understood yet. Herein, we combine density functional theory calculations, a multiscale structure reconstruction model, and kinetic Monte Carlo simulations to investigate the activity and structure sensitivity of Au NPs under different reaction conditions. The results indicate that increasing the partial pressure ratio of O_2 to CO leads to the decrease of optimal reaction temperature accompanied with the increase of performance. At low temperatures, the morphology of the NPs evolves to expose a higher proportion of (110) facets to promote the activity significantly. Moreover, the size dependence analysis suggests that O_2-rich conditions are favorable for small-sized NPs, while CO-rich conditions favor the large-sized NPs. These findings not only enrich our basic understanding of the structure–reactivity relationship and the origin of structure sensitivity in gold-catalysis, but provide a guide for rational design of Au catalysts.

Received 25th October 2023,
Accepted 24th November 2023

DOI: 10.1039/d3im00117b

rsc.li/icm

Keywords: Kinetic Monte Carlo; CO oxidation; Gold catalysis; Nanoparticles.

1 Introduction

Gold nanoparticles (NPs) exhibit extraordinary catalytic activities in various reactions under mild conditions, including CO oxidation,[1–3] water-gas shift reaction,[4] and partial oxidation of hydrocarbons.[5] Among these reactions, CO oxidation is of particular interest because Au NPs can catalyze this reaction at temperatures as low as 203 K.[1,2] It is generally agreed that the catalytic properties of Au NPs highly depend on their sizes and shapes.[3,6–10] Therefore, substantial efforts have been dedicated to synthesizing and characterizing Au NPs with well-defined shapes and sizes.[11–14] However, the situation becomes complicated due to the change in particle morphology under reaction conditions.[15,16] It poses a challenge to comprehensively investigate the structure–reactivity relationship taking the reaction-condition-driven particle reshaping into account.

In the past decade, several theoretical models based on density functional theory (DFT)[17] have contributed significant atomic-level insights into the structure sensitivity of Au NPs in CO oxidation.[18–23] These models were formulated upon small gold clusters or fixed high-symmetrical structures, *e.g.*, a classical truncated octahedral geometry. Due to the neglect of the influence of reaction environments on morphology, their ability to offer a comprehensive understanding of realistic catalytic activity is limited.

In this work, a density functional theory (DFT) based multiscale structural reconstruction (MSR) model[24–26] was used to construct the equilibrium structure of Au NPs in the size range of 3–10 nm under varying reaction conditions. Then, kinetic Monte Carlo (KMC) simulations were performed to evaluate the corresponding catalytic performance. This work focused on the investigation of freestanding single crystalline Au NPs, while exploring the effect of twinning[27,28] and the support oxide[6,18,29] on Au catalysis would be an interesting study in the future. Our results show that the activity is significantly influenced by the structural reconstruction induced by the reaction atmosphere. Furthermore, the size dependency of activity is intricately linked to the reaction conditions.

2 Results and discussion

2.1 Structure–reactivity relation

The shape evolution of 5 nm Au NPs at different temperatures and under changing partial pressure ratios of P_{O_2}/P_{CO} (1 bar total pressure) is shown in Fig. 1a. The

[a] *Key Laboratory of Interfacial Physics and Technology, Shanghai Institute of Applied Physics, Chinese Academy of Sciences, Shanghai 201800, China. E-mail: zhube@sari.ac.cn, gaoyi@sari.ac.cn*
[b] *University of Chinese Academy of Sciences, Beijing 100049, China*
[c] *Phonon Science Research Center for Carbon Dioxide, Shanghai Advanced Research Institute, Chinese Academy of Sciences, Shanghai 201210, China*
[d] *Key Laboratory of Low-Carbon Conversion Science & Engineering, Shanghai Advanced Research Institute, Chinese Academy of Sciences, Shanghai 201210, China*
† Electronic supplementary information (ESI) available. See DOI: https://doi.org/10.1039/d3im00117b

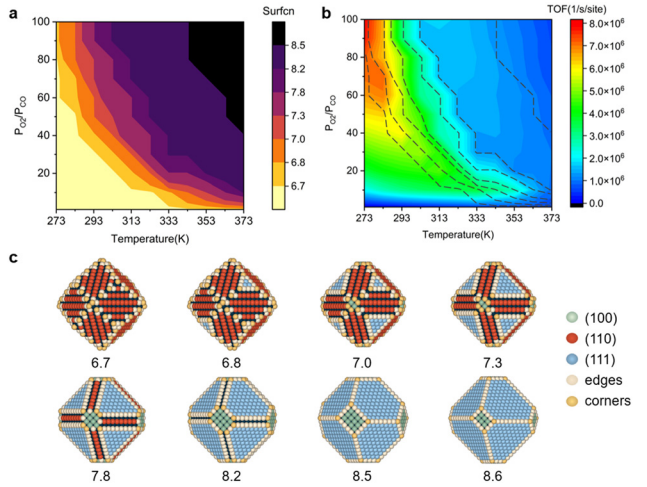

Fig. 1 (a) Contour plot of $\overline{CN}$s (b) TOFs for 5 nm Au NPs changing with the temperature and partial pressure ratio (P_{total} = 1 bar). Contour lines of $\overline{CN}$s are marked by black dashed curves as guides to the eyes; (c) typical structures with different $\overline{CN}$.

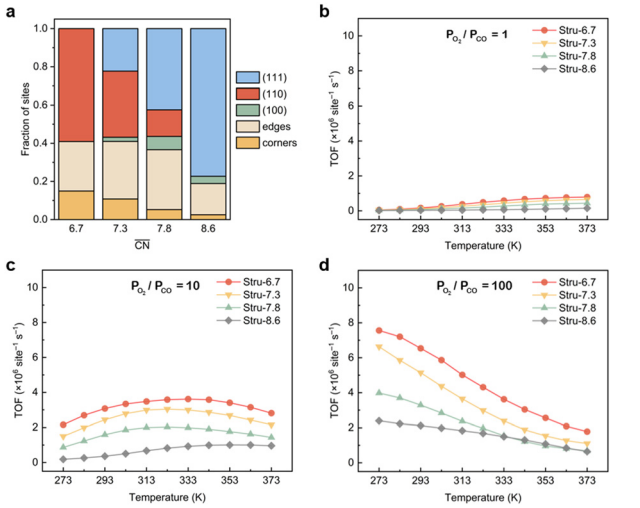

Fig. 2 (a) Surface site fractions of (111), (110), (100), edges and corners of Au NPs with different $\overline{CN}$; TOFs as a function of temperature at P_{total} = 1 bar with P_{O_2}/P_{CO} = 1 (b), 10 (c), and 100 (d) for Au NPs with different $\overline{CN}$.

temperature ranged from 273 to 373 K and P_{O_2}/P_{CO} ranged from 1 to 100. The NPs with different shapes are distinguished by the average coordination number of surface atoms ($\overline{CN}$).[30] Typical structures with different $\overline{CN}$s are illustrated in Fig. 1c. In general, when the temperature is higher than 343 K and P_{O_2}/P_{CO} is larger than 60, the adsorption of gas on the Au NPs becomes difficult, and the corresponding structure ($\overline{CN}$ = 8.6) is close to the structure under vacuum (Fig. 1). With a decrease in temperature and O_2 partial pressure, the fraction of the (110) facet increases, while the fraction of the (111) facet decreases. This change is attributed to the different coverage evolution on different facets.[25] The coverage of CO increases rapidly on the (110) facet due to its stronger adsorption energy (Table S1†), resulting in the rapid decrease of the interface energy of the (110) facet, which further leads to a change of equilibrium morphology. More details can be found in Section 4.2 and our previous works.[24–26] The contour plot of TOFs of these NPs under corresponding reaction conditions shows that the catalytic activity is significantly enhanced under low temperature and O_2-rich conditions (Fig. 1b). To demonstrate how structure evolution affects the activity clearly, contour lines of $\overline{CN}$s are marked by black dashed curves in Fig. 1b. It can be observed that there is partial overlap between the contour lines of $\overline{CN}$ and TOFs, showing the shape-sensitivity of this system. The 110-dominant structures ($\overline{CN} \leq 7.0$) exhibit high activity (TOF $\geq 5.6 \times 10^6$ per site per s) when P_{O_2}/P_{CO} is higher than 50, while the (111)-dominated structures ($\overline{CN} \geq 8.5$) always show low activity (TOF $\leq 1.8 \times 10^6$ per site per s).

To disentangle the contribution of morphology changes and reaction conditions to the catalytic activity, Stru-6.7, Stru-7.3, Stru-7.8, and Stru-8.6 were chosen to obtain the fixed-structure contour plots of TOFs (Fig. S3†). Surface site fractions of these four structures are presented in Fig. 2a and their TOFs as a function of temperature were compared under P_{O_2}/P_{CO} = 1, 10, and 100, respectively (Fig. 2b–d). It can be observed that a higher proportion of (110) facet sites is generally beneficial for catalytic reactions in our studied conditions, and the TOFs of different structures exhibit similar trends. At P_{O_2}/P_{CO} = 1, the TOFs are below 0.8×10^6 per site per s and increase slightly with the increase of temperature for all NPs. At P_{O_2}/P_{CO} = 10, the TOFs initially increase and then decrease as the temperature increases. The maximum TOF values are 3.6×10^6 per site per s at 333 K, 3.0×10^6 per site per s at 323 K, 2.0×10^6 per site per s at 323 K, and 1.0×10^6 per site per s at 353 K for Stru-6.7, Stru-7.3, Stru-7.8, and Stru-8.6, respectively. At P_{O_2}/P_{CO} = 100, the TOFs of NPs are highest at 273 K ranging from 2.4×10^6 to 7.6×10^6 per site per s and decline at higher temperatures. The results indicate that as P_{O_2}/P_{CO} increases, the optimal temperature for the highest TOF decreases. Meanwhile, the value of the highest TOF increases. This is because the binding energy of CO is about 0.45–0.57 eV stronger than that of O_2 (Fig. S1†). Therefore, the increase of O_2 partial pressure eliminates the risk of CO poisoning at low temperatures and facilitates the adsorption of O_2 (Fig. S4†), leading to a higher activity.

2.2 Site-specific activity

To understand the activity changes in detail, Au NPs with $\overline{CN}$ = 7.3, which possess a relatively uniform site distribution, were chosen as an example to show the site-specific contributions to TOFs and CO coverages at atmosphere pressure with P_{O_2}/P_{CO} = 1, 10, and 100 (Fig. 3). The plots of the other three structures are displayed in Fig. S5–S7.† Generally, the activities of NPs reach the maximum as their coverage of CO is around 0.60. This results in the decrease of

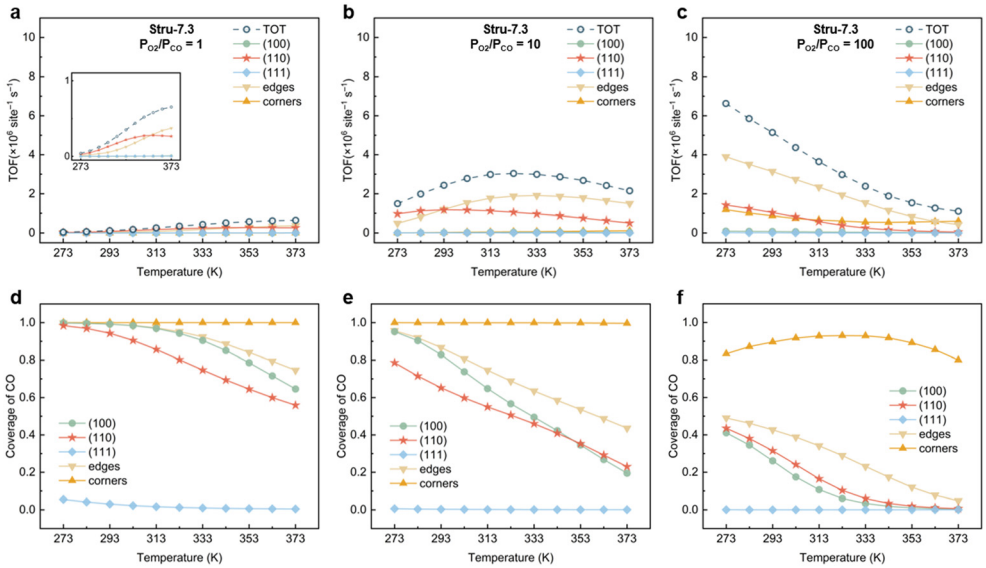

Fig. 3 Site-specific contributions to TOFs and coverages of CO for Au NPs with Stru-7.3 under P_{O_2}/P_{CO} = 1 (a, d), 10 (b, e), and 100 (c, f).

the optimal temperature with the increase of O_2 partial pressure. At P_{O_2}/P_{CO} = 1 (Fig. 3a and d), the overly adsorbed CO poisoned all sites except the (111) facet at 273 K, causing a very low total TOF (4.2×10^4 per site per s). The increase of temperature alleviates the CO poisoning on (110) facets first, followed by the edges and (100) facet sites, resulting in a monotonic increase in activity. At P_{O_2}/P_{CO} = 10 (Fig. 3b and e), the activity of the (110) facet increases first and then declines as the temperature increases. The maximum activity of 1.2×10^6 per site per s is achieved at 293 K, with a CO coverage of 0.65. For edge sites, the optimal temperature is higher (333 K), with a maximum activity of 1.9×10^6 per site per s and a CO coverage of 0.63. At P_{O_2}/P_{CO} = 100 (Fig. 3c and f), corner sites are protected from poisoning and maintained relatively stable activity at around $7.2 \pm 2.1 \times 10^5$ per site per s from 273 to 373 K, whereas the activity of (110) facets declines from 1.4×10^6 to 4.9×10^4 per site per s and the activity of edge sites declines from 3.9×10^6 to 4.2×10^5 per site per s. Overall, the (110) facet and edge sites dominate the reactions except at 373 K with P_{O_2}/P_{CO} = 100, in which condition corner sites make the major contributions. The contributions of (100) and (111) to TOFs are negligible under all conditions. Decreasing the temperature and increasing the P_{O_2}/P_{CO} promote the reaction and increase the exposure of active (110) facet sites, thereby further enhancing the activity of Au NPs.

2.3 Size effect

It is suggested that the critical size for finite-size effects of Au is about 2.7 nm.[31] To compare with the experiment,[3] the activities of Au NPs in the size range of 3–10 nm constructed by the MSR model were investigated at 350 K at a total pressure of 0.053 bar with P_{O_2}/P_{CO} = 5 (Fig. 4). In this condition, Au nanoparticles exhibited a classical truncated octahedral geometry. KMC calculations overestimated the activity by approximately 3 orders of magnitude as compared to the experimental results, which arises from the use of the PBE functional and scaling relationship.[32] Nevertheless, a similar trend was obtained. Yellow dashed lines in Fig. 4 show the fraction of edges and corners for particle sizes. It suggests that the activity dependence on the particle size under experimental conditions is closely correlated with the fractions of edges and corners. This finding is coincident with previous studies which suggested that the main effect of decreasing the size of Au NPs is the increase of the proportion of low-coordinated Au atoms.[7,33,34]

However, as discussed in the preceding sections, at certain temperatures and partial pressure ratios, adsorbates can induce the structural reconstruction of gold nanoparticles,

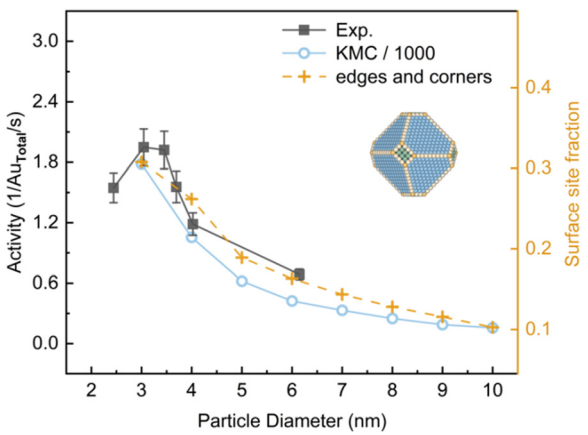

Fig. 4 The activity for CO oxidation at 350 K under 40 Torr with P_{O_2}/P_{CO} = 5 as a function of particle diameter of the Au NPs. Experimental data from ref. 3. Activity is expressed as (product molecules) × (total Au atoms)$^{-1}$ × s^{-1}. Reaction-condition-dependent structure of 5 nm Au NP is shown in inserts.

resulting in the exposure of the active (110) surface at atmospheric pressure. Under these conditions, the catalytic activity of Au NPs should exhibit different size dependence. To validate it, the TOFs for Au NPs with reaction-condition-dependent structure in the size range of 3–10 nm were obtained at different temperatures and partial pressure ratios P_{O_2}/P_{CO} with the fixed total pressure of 1 bar (Fig. S8†). The size effects were measured by the TOF ratio between 10 nm and 3 nm particles (TOF_{10}/TOF_3) and were plotted as a heatmap (Fig. 5a). Three representative size-dependent TOF trends are shown in Fig. 5b, and the corresponding 5 nm particle geometries colored according to the TOF at specific sites are illustrated in Fig. 5c. At high temperature and high P_{O_2}/P_{CO} (*e.g.*, T = 373 K, P_{O_2}/P_{CO} = 100), only edge and corner sites are active, resulting in a sharp decrease when the diameter increases, similar to Fig. 4. However, at low temperature and low P_{O_2}/P_{CO} (*e.g.*, T = 273 K, P_{O_2}/P_{CO} = 1), the (110) facet sites are the only active sites, because the edges and corners are poisoned. So, the TOF grows with particle size, similar to the effect for Pt particles.[10,35] Notably, at low temperature and high P_{O_2}/P_{CO} (*e.g.*, T = 273 K, P_{O_2}/P_{CO} = 100), all sites are active. Although the edge and corner sites exhibit higher intrinsic activities, the (110) facet sites also make a large contribution to the total activity owing to the large area, especially for large NPs. This allows the particle to maintain a relatively high activity even at a size of 10 nm, which is about half the activity of a 3 nm particle.

From the above results and discussion, we show that when the effect of CO poisoning is strong, the particle activity is unusually proportional to its size. When the particle is not poisoned by CO, its activity increases with the decrease of size. These findings may explain why the optimal active size of Au NPs is around 3 nm.[3,9] When the size of the Au NP becomes extremely small (1–2 nm), its interaction with CO will be enhanced due to the finite size effect.[31] This could induce the CO poisoning effect and thus inversely reduce the activity.

3 Conclusions

In conclusion, we investigated the CO oxidation over Au NPs with reaction-condition dependent structures at sizes ranging from 3 to 10 nm at different temperatures and partial pressure ratios P_{O_2}/P_{CO} with the fixed total pressure of 1 bar. The temperature ranged from 273 to 373 K and P_{O_2}/P_{CO} ranged from 1 to 100. The results suggested that with the increase in P_{O_2}/P_{CO}, the optimal temperature decreases from 373 to 273 K and the highest TOF increases. This is because the reaction is limited by O_2 adsorption. At low temperatures and under O_2-rich conditions, all sites exhibit high activity without being poisoned by CO. Also, under these conditions, a higher proportion of (110) facets is exposed induced by adsorbates, making a substantial contribution to total activity together with corners and edges, especially for the large-size particles. This work provides a comprehensive understanding of the structure sensitivity for Au NPs in CO oxidation. Also, it provides a promising way to further catalyst design based on atomic-level understanding.

4 Computational methods

The Langmuir–Hinshelwood mechanism involving the formation of an OCOO intermediate[36] was considered to model the Au-catalyzed CO oxidation:

$$CO(g) + * \rightleftharpoons CO* \quad (R1)$$

$$O_2(g) + * \rightleftharpoons O_2^* \quad (R2)$$

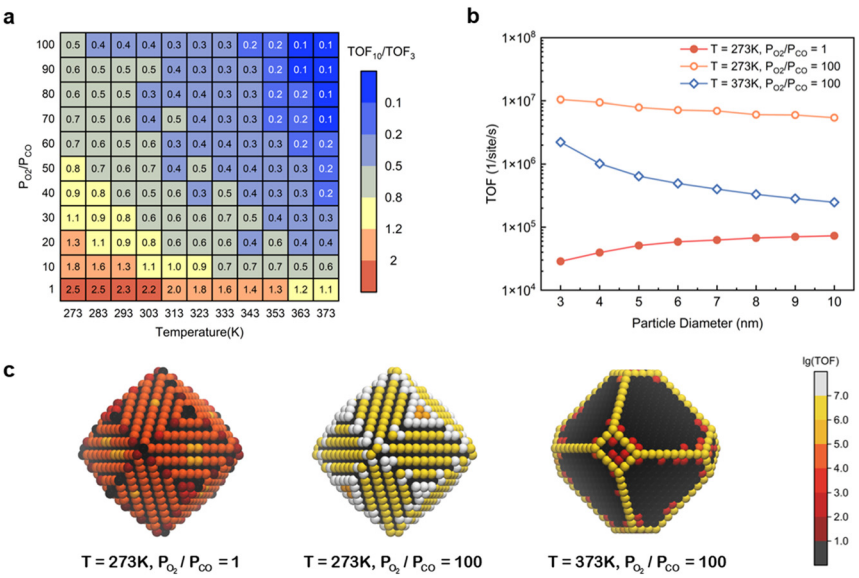

Fig. 5 (a) Heatmap of TOF_{10}/TOF_3 changing with the temperature and partial pressure ratio with a fixed total pressure of 1 bar; (b) three representative size-dependent TOF trends; (c) 5 nm Au NPs colored according to the TOF at specific sites.

$$CO^* + O_2^* \rightleftharpoons OCOO^* \quad \text{(R3)}$$

$$OCOO^* \rightarrow CO_2(g) + O^* + * \quad \text{(R4)}$$

$$CO(g) + O^* \rightarrow CO_2(g) + * \quad \text{(R5)}$$

$$CO^* + * \rightarrow * + CO^* \text{ (diffusion)} \quad \text{(R6)}$$

$$O_2^* + * \rightarrow * + O_2^* \text{(diffusion)} \quad \text{(R7)}$$

$$O^* + * \rightarrow * + O^* \text{ (diffusion)} \quad \text{(R8)}$$

Here, an asterisk * stands for a free site in the surface. And the surface species are labelled with superscript asterisks. For simplicity, the reaction product (CO_2) was considered to desorb immediately after its formation and the diffusion of the reaction intermediate (OCOO) was neglected.

4.1 Density functional theory

DFT calculations were performed using the Vienna *Ab initio* Simulation Package (VASP) in the projector-augmented wave (PAW) scheme.[37–39] The electronic states were expanded on a plane wave basis with a cutoff of 400 eV. The generalized gradient approximation (GGA) with the Perdew–Burke–Ernzerhof (PBE) functional was adopted.[40] Structures were optimized until all forces were below 0.05 eV Å^{-1}.

Surface tensions under vacuum were extracted[41] from the energies of a series of (1 × 1) slab models with increasing layers from 6 to 20. For surface species, (4 × 4), (2 × 2), and (1 × 1) slab models were constructed to calculate adsorption energies and lateral interactions between adsorbates.[25] Each model contained 6 atomic layers, where the positions of 2 bottom layers were fixed. The vacuum space of 15 Å was set along the *z*-axis. The *k*-point grids[42] were set to be (3 × 3 × 1), (6 × 6 × 1), and (10 × 10 × 1) for the (4 × 4), (2 × 2), (1 × 1) slab models, respectively. All calculated results are listed in Tables S1 and S2.†

4.2 MSR model

By combing the Fowler–Guggenheim (F–G) adsorption isotherm[43] and Wulff theorem,[44] the equilibrium shape of Au NPs under reaction conditions can be constructed based on the interface tension[24–26] of three low-index facets ((100), (110), (111)):

$$\gamma_{hkl}^{\text{int}} = \gamma_{hkl} + [\theta_{CO}(E_{CO} - z(w_{CO-CO}\theta_{CO} + w_{CO-O_2}\theta_{O_2})) + \theta_{O_2}(E_{O_2} - z(w_{CO-O_2}\theta_{CO} + w_{O_2-O2}\theta_{O_2}))]/A_{at} \quad (1)$$

Here, γ_{hkl} is the surface tension of the (*hkl*) facet under vacuum, E_{CO} and E_{O_2} are the adsorption energy of CO and O_2 on this facet, θ is the coverage of the corresponding adsorbates, z is the number of nearest neighbor sites, w is the lateral interaction between two neighboring adsorbates, and A_{at} is the surface area per atom. Considering the short lifetime of intermediates, their coverage on the NP during reaction has been neglected. The coverages of CO and O_2 on each facet can be derived by solving the following equations, respectively:

$$P_{CO}K_{CO} = \frac{\theta_{CO}}{1-(\theta_{CO}+\theta_{O_2})}\exp\left(-\frac{z(w_{CO-CO}\theta_{CO} + w_{CO-O_2}\theta_{O_2})}{k_BT}\right) \quad (2)$$

$$P_{O_2}K_{O_2} = \frac{\theta_{O_2}}{1-(\theta_{CO}+\theta_{O_2})}\exp\left(-\frac{z(w_{CO-O_2}\theta_{CO} + w_{O_2-O_2}\theta_{O_2})}{k_BT}\right) \quad (3)$$

where k_B is the Boltzmann constant, and K is the equilibrium constant defined as:

$$K_{CO} = \exp\left(-\frac{E_{CO} - T(S_{ads,CO} - S_{gas,CO})}{k_BT}\right) \quad (4)$$

$$K_{O_2} = \exp\left(-\frac{E_{CO} - T(S_{ads,O_2} - S_{gas,O_2})}{k_BT}\right) \quad (5)$$

where S_{ads} represents the entropy of the adsorbed species, which is assumed to be negligible. S_{gas} represents the entropy of gas-phase species, which is obtained from the NIST-JANAF thermochemical tables.[45]

4.3 Kinetic Monte Carlo

KMC simulation with the direct method (DM)[46–48] was adopted to study the catalytic activities of Au NPs under *operando* conditions. In the DM, the time interval of each KMC step is evaluated by the total rate constant ($k_{tot} = \sum k_{event}$):

$$\Delta t = -\frac{\ln(u_1)}{k_{tot}} \quad (6)$$

Here u_1 is a random number on the interval (0, 1]. The event occurring at this step is chosen with a probability proportional to its rate constant and determined by another random number u_2.

The rate constant for adsorption is obtained from collision theory, assuming a zero-activation energy:

$$k_{ads,i} = \frac{s_i A_{at} P_i}{\sqrt{2\pi M_i k_B T}} \quad (7)$$

where the subscript i denotes the species, M denotes its molecular mass and s denotes the sticking coefficient. On the facet sites, the sticking coefficient is assumed to be 0.9 for CO and 0.1 for O_2.[49,50] While on edges and corners they are both assumed to be 1.0. To ensure thermodynamic equilibrium, the corresponding desorption rate constant is obtained from $k_{ads,i}$ and equilibrium constant K_i:

$$k_{des,i} = \frac{k_{ads,i}}{K_i P_i} \quad (8)$$

The rate constants for reaction and diffusion events are obtained from transition state theory (TST):

$$k_{\text{event}} = \frac{k_B T}{h}\left(\frac{Z^{TS}}{Z^{IS}}\right)\exp\left(\frac{-E_a^{\text{event}}}{k_B T}\right) \quad (9)$$

Here, h is the plank's constant. Z^{TS} and Z^{IS} are the partition function of the transition state and initial state, which are assumed to be equal in the simulation. E_a^{event} is the activation energy. For the reaction $[CO^* + O_2^* \rightleftharpoons OCOO^*]$ and $[OCOO^* \rightarrow CO_2(g) + O^* + *]$, the activation energy is evaluated by the BEP relations and scaling relation fitted based on ref. 19–21 and 51–53 (Fig. S1c–e†). For the reaction $[CO(g) + O^* \rightarrow CO_2(g) + *]$, the activation energy is assumed to be 0.1 eV following the previous study.[21] For diffusion, we increase the diffusion barrier to 0.6 eV for all adsorbates to accelerate KMC simulation while ensuring convergence (Fig. S2†).

To ensure the reliability of the results, all KMC simulations were performed for a total of 100 million steps. The turnover frequency (TOF) of the reaction was calculated as the reaction rate per surface site over the last 10 million steps.

Author contributions

Y. G. initiated the project. Y. G. and B. Z. supervised the project. L. Y. and Y. H. performed the calculations. L. Y. performed the simulations and data analysis. L. Y. wrote the original draft. Y. G. and B. Z. revised the manuscript. All authors have given approval to the final version of the manuscript.

Conflicts of interest

The authors declare no competing financial interest.

Acknowledgements

The work is supported by the National Natural Science Foundation of China (12174408), Natural Science Foundation of Shanghai (22JC1404200), and the Foundation of Key Laboratory of Low-Carbon Conversion Science & Engineering, Shanghai Advanced Research Institute, Chinese Academy of Sciences (KLLCCSE-202201Z, SARI, CAS). B. Z. acknowledges the financial support of Key Research Program of Frontier Sciences, CAS, Grant No. ZDBS-LY-7012. All calculations were performed at National Supercomputer Centers in Tianjin, Shanghai and Guangzhou.

References

1 M. Haruta, T. Kobayashi, H. Sano and N. Yamada, Novel gold catalysts for the oxidation of carbon monoxide at a temperature far below 0 °C, *Chem. Lett.*, 1987, **16**, 405–408.
2 M. Haruta, S. Tsubota, T. Kobayashi, H. Kageyama, M. J. Genet and B. Delmon, Low-temperature oxidation of CO over gold supported on TiO_2, α-Fe_2O_3, and Co_3O_4, *J. Catal.*, 1993, **144**, 175–192.
3 M. Valden, X. Lai and D. W. Goodman, Onset of catalytic activity of gold clusters on titania with the appearance of nonmetallic properties, *Science*, 1998, **281**, 1647–1650.
4 D. Andreeva, V. Idakiev, T. Tabakova and A. Andreev, Low-temperature water–gas shift reaction over Au/α-Fe_2O_3, *J. Catal.*, 1996, **158**, 354–355.
5 M. D. Hughes, Y.-J. Xu, P. Jenkins, P. McMorn, P. Landon, D. I. Enache, A. F. Carley, G. A. Attard, G. J. Hutchings, F. King, E. H. Stitt, P. Johnston, K. Griffin and C. J. Kiely, Tunable gold catalysts for selective hydrocarbon oxidation under mild conditions, *Nature*, 2005, **437**, 1132–1135.
6 M. Haruta, Size- and support-dependency in the catalysis of gold, *Catal. Today*, 1997, **36**, 153–166.
7 N. Lopez, T. Janssens, B. Clausen, Y. Xu, M. Mavrikakis, T. Bligaard and J. Norskov, On the origin of the catalytic activity of gold nanoparticles for low-temperature CO oxidation, *J. Catal.*, 2004, **223**, 232–235.
8 M. S. Chen and D. W. Goodman, Structure–activity relationships in supported Au catalysts, *Catal. Today*, 2006, **111**, 22–33.
9 I. Laoufi, M.-C. Saint-Lager, R. Lazzari, J. Jupille, O. Robach, S. Garaudée, G. Cabailh, P. Dolle, H. Cruguel and A. Bailly, Size and catalytic activity of supported gold nanoparticles: An in operando study during Co oxidation, *J. Phys. Chem. C*, 2011, **115**, 4673–4679.
10 S. Cao, F. (Feng) Tao, Y. Tang, Y. Li and J. Yu, Size- and shape-dependent catalytic performances of oxidation and reduction reactions on nanocatalysts, *Chem. Soc. Rev.*, 2016, **45**, 4747–4765.
11 Y. Sun and Y. Xia, Shape-controlled synthesis of gold and silver nanoparticles, *Science*, 2002, **298**, 2176–2179.
12 A. R. Tao, S. Habas and P. Yang, Shape control of colloidal metal nanocrystals, *Small*, 2008, **4**, 310–325.
13 R. P. Briñas, M. Hu, L. Qian, E. S. Lymar and J. F. Hainfeld, Gold nanoparticle size controlled by polymeric Au(I) thiolate precursor size, *J. Am. Chem. Soc.*, 2007, **130**, 975–982.
14 P. Suchomel, L. Kvitek, R. Prucek, A. Panacek, A. Halder, S. Vajda and R. Zboril, Simple size-controlled synthesis of Au nanoparticles and their size-dependent catalytic activity, *Sci. Rep.*, 2018, **8**, 4589.
15 T. Uchiyama, H. Yoshida, Y. Kuwauchi, S. Ichikawa, S. Shimada, M. Haruta and S. Takeda, Systematic morphology changes of gold nanoparticles supported on CeO_2 during CO oxidation, *Angew. Chem., Int. Ed.*, 2011, **50**, 10157–10160.
16 N. Kamiuchi, K. Sun, R. Aso, M. Tane, T. Tamaoka, H. Yoshida and S. Takeda, Self-activated surface dynamics in gold catalysts under reaction environments, *Nat. Commun.*, 2018, **9**, 2060.
17 P. Hohenberg and W. Kohn, Inhomogeneous electron gas, *Phys. Rev.*, 1964, **136**, B864–B871.
18 T. V. W. Janssens, B. S. Clausen, B. Hvolbæk, H. Falsig, C. H. Christensen, T. Bligaard and J. K. Nørskov, Insights into the reactivity of supported Au nanoparticles: Combining theory and experiments, *Top. Catal.*, 2007, **44**, 15–26.
19 H. Li, L. Li, A. Pedersen, Y. Gao, N. Khetrapal, H. Jónsson and X. C. Zeng, Magic-number gold nanoclusters with

diameters from 1 to 3.5 nm: Relative stability and catalytic activity for CO oxidation, *Nano Lett.*, 2014, **15**, 682–688.
20 J. X. Liu, I. A. W. Filot, Y. Su, B. Zijlstra and E. J. M. Hensen, Optimum particle size for gold-catalyzed CO oxidation, *J. Phys. Chem. C*, 2018, **122**, 8327–8340.
21 H. Xu, D. Cheng, Y. Gao and X. C. Zeng, Assessment of catalytic activities of gold nanoclusters with simple structure descriptors, *ACS Catal.*, 2018, **8**, 9702–9710.
22 F. H. Kaatz, D. Yu. Murzin and A. Bultheel, Coordination-dependent kinetics in the catalysis of gold nanoclusters, *ACS Catal.*, 2021, **11**, 9073–9085.
23 Y. Gao, N. Shao, Y. Pei, Z. Chen and X. C. Zeng, Catalytic activities of subnanometer gold clusters (Au_{16}–Au_{18}, Au_{20}, and Au_{27}–Au_{35}) for CO oxidation, *ACS Nano*, 2011, **5**, 7818–7829.
24 B. Zhu, Z. Xu, C. Wang and Y. Gao, Shape evolution of metal nanoparticles in water vapor environment, *Nano Lett.*, 2016, **16**, 2628–2632.
25 J. Meng, B. Zhu and Y. Gao, Shape evolution of metal nanoparticles in binary gas environment, *J. Phys. Chem. C*, 2018, **122**, 6144–6150.
26 B. Zhu, J. Meng, W. Yuan, X. Zhang, H. Yang, Y. Wang and Y. Gao, Reshaping of metal nanoparticles under reaction conditions, *Angew. Chem., Int. Ed.*, 2020, **59**, 2171–2180.
27 X. Ma, F. Lin, X. Chen and C. Jin, Unveiling Growth Pathways of Multiply Twinned Gold Nanoparticles by *In Situ* Liquid Cell Transmission Electron Microscopy, *ACS Nano*, 2020, **14**, 9594–9604.
28 E. yakout El koraychy, C. Roncaglia, D. Nelli, M. Cerbelaud and R. Ferrando, Growth mechanisms from tetrahedral seeds to multiply twinned Au nanoparticles revealed by atomistic simulations, *Nanoscale Horiz.*, 2022, **7**, 883–889.
29 D. Widmann and R. J. Behm, Activation of Molecular Oxygen and the Nature of the Active Oxygen Species for CO Oxidation on Oxide Supported Au Catalysts, *Acc. Chem. Res.*, 2014, **47**, 740–749.
30 X. Duan, X. Y. Li, B. Zhu and Y. Gao, Identifying the morphology of Pt nanoparticles for the optimal catalytic activity towards CO oxidation, *Nanoscale*, 2022, **14**, 17754–17760.
31 J. Kleis, J. Greeley, N. A. Romero, V. A. Morozov, H. Falsig, A. H. Larsen, J. Lu, J. J. Mortensen, M. Dułak, K. S. Thygesen, J. K. Nørskov and K. W. Jacobsen, Finite size effects in chemical bonding: From small clusters to solids, *Catal. Lett.*, 2011, **141**, 1067–1071.
32 Y. Yang, T. Shen and X. Xu, Understanding the source of error in first-principles-based micro-kinetic modeling: Density functional theory calculations *versus* the mean-field approximation, *J. Phys. Chem. C*, 2023, **127**, 9631–9639.
33 X. Bokhimi, R. Zanella and A. Morales, Au/rutile catalysts: Effect of support dimensions on the gold crystallite size and the catalytic activity for CO oxidation, *J. Phys. Chem. C*, 2007, **111**, 15210–15216.
34 K. Qian, L. Luo, H. Bao, Q. Hua, Z. Jiang and W. Huang, Catalytically active structures of SiO_2-supported Au nanoparticles in low-temperature CO oxidation, *Catal. Sci. Technol.*, 2013, **3**, 679–687.
35 M. Jørgensen and H. Grönbeck, Scaling relations and kinetic Monte Carlo simulations to bridge the materials gap in heterogeneous catalysis, *ACS Catal.*, 2017, **7**, 5054–5061.
36 Z. P. Liu, P. Hu and A. Alavi, Catalytic role of gold in gold-based catalysts: A density functional theory study on the CO oxidation on gold, *J. Am. Chem. Soc.*, 2002, **124**, 14770–14779.
37 G. Kresse and J. Furthmüller, Efficiency of *ab initio* total energy calculations for metals and semiconductors using a plane-wave basis set, *Comput. Mater. Sci.*, 1996, **6**, 15–50.
38 G. Kresse and J. Furthmüller, Efficient iterative schemes for *ab initio* total-energy calculations using a plane-wave basis set, *Phys. Rev. B: Condens. Matter Mater. Phys.*, 1996, **54**, 11169–11186.
39 P. E. Blöchl, Projector augmented-wave method, *Phys. Rev. B: Condens. Matter Mater. Phys.*, 1994, **50**, 17953–17979.
40 J. P. Perdew, K. Burke and M. Ernzerhof, Generalized gradient approximation made simple, *Phys. Rev. Lett.*, 1996, **77**, 3865–3868.
41 V. Fiorentini and M. Methfessel, Extracting convergent surface energies from slab calculations, *J. Phys.: Condens. Matter*, 1996, **8**, 6525–6529.
42 H. J. Monkhorst and J. D. Pack, Special points for Brillouin-zone integrations, *Phys. Rev. B: Solid State*, 1976, **13**, 5188–5192.
43 R. H. Fowler and E. A. Guggenheim, *Statistical Thermodynamics*, Cambridge University Press, Cambridge, U. K., 1939.
44 G. Wulff, On the question of speed of growth and dissolution of crystal surfaces, *Z. Kristallogr. Mineral.*, 1901, **34**, 450–530.
45 M. W. Chase, *NIST-JANAF Thermochemical Tables*, American Institute of Physics, 4th edn, 1998.
46 A. P. J. Jansen, *An Introduction to Kinetic Monte Carlo Simulations of Surface Reactions*, Springer, Berlin, Heidelberg, 2012.
47 D. T. Gillespie, A general method for numerically simulating the stochastic time evolution of coupled chemical reactions, *J. Comput. Phys.*, 1976, **22**, 403–434.
48 D. T. Gillespie, Exact stochastic simulation of coupled chemical reactions, *J. Phys. Chem.*, 1977, **81**, 2340–2361.
49 J. M. Gottfried, K. J. Schmidt, S. L. M. Schroeder and K. Christmann, Adsorption of carbon monoxide on Au(1 1 0)-(1 × 2), *Surf. Sci.*, 2003, **536**, 206–224.
50 Y. Han, X.-Y. Li, B. Zhu and Y. Gao, Unveiling the Au surface reconstruction in a CO environment by surface dynamics and *Ab initio* thermodynamics, *J. Phys. Chem. A*, 2022, **126**, 6538–6547.
51 H. Li and J. Ho, Theoretical calculations on the oxidation of CO on Au_{55}, $Ag_{13}Au_{42}$, $Au_{13}Ag_{42}$, and Ag_{55} clusters of nanometer size, *J. Phys. Chem. C*, 2012, **116**, 13196–13201.
52 J. L. C. Fajín, A. S. Moura and M. N. D. S. Cordeiro, First-principles-based kinetic Monte Carlo simulations of CO oxidation on catalytic Au(110) and Ag(110) surfaces, *Phys. Chem. Chem. Phys.*, 2021, **23**, 14037–14050.
53 W. An, Y. Pei and X. C. Zeng, CO oxidation catalyzed by single-walled helical gold nanotube, *Nano Lett.*, 2007, **8**, 195–202.